ACS OMEGA

http://pubs.acs.org/journal/acsodf

Article

Bactericidal Action and Industrial Dye Degradation of Graphene Oxide and Polyacrylic Acid-Doped SnO_2 Quantum Dots: *In Silico* Molecular Docking Study

Saira Riaz, Muhammad Ikram,* Sadia Naz, Anum Shahzadi, Walid Nabgan,* Anwar Ul-Hamid, Ali Haider, Junaid Haider, and Ali Al-Shanini*

Cite This: *ACS Omega* 2023, 8, 5808−5819

Read Online

ACCESS | Metrics & More | Article Recommendations | Supporting Information

ABSTRACT: The present work demonstrates the systematic incorporation of different concentrations of graphene oxide (GO) into a fixed amount of polyacrylic acid (PAA)-doped SnO_2 quantum dots (QDs) through a co-precipitation approach. The research aimed to evaluate the catalytic and antibacterial actions of GO/PAA-SnO_2 QDs. Moreover, optical properties, surface morphologies, crystal structures, elemental compositions, and d-spacings of prepared QDs were examined. X-ray diffraction patterns revealed the tetragonal configuration of SnO_2, and the crystallinity of QDs was suppressed upon dopants verified by the SAED patterns. Electronic spectra identified the blue shift by incorporating GO and PAA led to a reduction in band gap energy. Fourier transform infrared spectra showed the existence of rotational and vibrational modes associated with the functional groups during the synthesis process. A drastic increase in the catalytic efficacy of QDs was observed in the neutral medium by including dopants, indicating that GO/PAA-SnO_2 is a promising catalyst. GO/PAA-SnO_2 showed strong bactericidal efficacy against *Escherichia coli* (*E. coli*) at higher GO concentrations. Molecular docking studies predicted the given nanocomposites, i.e., SnO_2, PAA-SnO_2, and GO/PAA-SnO_2, as potential inhibitors of beta-lactamase$_{E.\ coli}$ and DNA gyrase$_{E.\ coli}$.

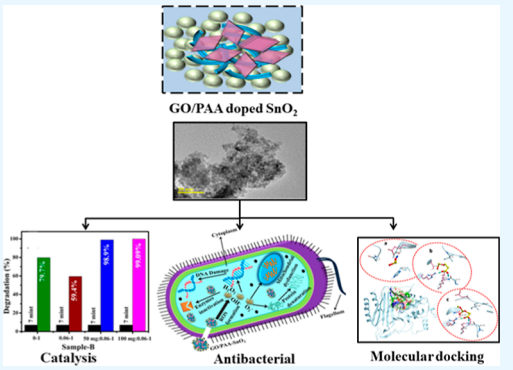

Downloaded via 84.88.201.34 on February 13, 2025 at 17:39:12 (UTC).
See https://pubs.acs.org/sharingguidelines for options on how to legitimately share published articles.

1. INTRODUCTION

Urbanization and fast industrialization are responsible for the discharge of many toxic insoluble organic and inorganic impurities (heavy metals and dyes etc.), destroying aquatic life, animals, and plants.[1,2] According to the World Health Organization (WHO), ∼2.3 million people die annually from polluted water that causes diseases like typhoid, diarrhea, cholera, hepatitis, and cancer.[3,4] Per annum, 1/10th million different dyes are employed, 10−15% of which are discharged directly and indirectly into the environment, causing havoc to life.[4,5] Fabric and paper industries apply different dyes; most of the dyes are aromatic compounds,[6] and two major cationic dyes are methylene blue (MB)[7] and rhodamine blue (RhB).[8] Herein, MB is adopted and explored because of its toxicity, extensive usage, and high commitment to biotic degradation.[9]

To remove impurities from water, different methods like ozonation,[10] membrane filtration,[11] adsorption,[12] catalytic reduction, and so forth[13,14] have been used. But catalytic reduction has a great impact showing good catalytic activity, affordability, and high thermal stability.[15−17] Nanomaterials possess fast adsorption, catalytic activity, and solubility attributed to the large surface area and small size. Different nanomaterials have been used to remove organic pollutants, inorganic anions, and various types of bacteria from water.[18] Using water-containing bacteria causes diseases, such as eye infection, respiratory tract irritation, skin irritation, and mastitis.[19] Mastitis has a significant economic impact on dairy products. Different factors, including host, environment, seasons, and specific agent parasites, such as *Staphylococcus Aureus* (*S. aureus*) and *Escherichia Coli* (*E. coli*) are responsible for it.[20,21]

Metal−organic frameworks (MOFs) and covalent organic frameworks have been considered as two types of organic materials, in the last few decades, which can be easily made and designed due to their properties.[22] In recent years, researchers have found great interest in semiconductor nanomaterials because of their remarkable physical and chemical properties, high surface area, and less toxicity. MOFs or porous coordination polymers are crystalline porous materials composed of inorganic metal nodes linked by organic linkers

Received: November 21, 2022
Accepted: January 25, 2023
Published: February 6, 2023

© 2023 The Authors. Published by American Chemical Society

via coordination bonds.[23,24] Different types of semiconductor nanomaterials, such as Li_2O_3, SnO_2, ZnO, MnO_4, CdS, and so forth, are applicable; SnO_2 has attracted great attention for purifying drain water. SnO_2 is an n-type semiconductor with a wide band gap (E_g = 3.6 eV)[25] and has remarkable properties, such as electrical conductivity rechargeability, high transmittance in the ultraviolet (UV)−visible (vis) region, low toxicity, and negligible biological effects. Various methods for degrading dyes have been adopted for synthesizing metal oxides, including hydrothermal, co-precipitation, sol−gel, and so forth.[26] From these methods, the co-precipitation technique is used as it is eco-friendly, inexpensive, energy-efficient, and easy to use with a short preparation time.[27]

However, SnO_2 has the limitation of a high recombination rate. To overcome this problem, different polymers like polyvinyl alcohol (PVA), polyvinylpyrrolidone (PVP), and polyacrylic acid (PAA) are used, which have great influence as dopants because of their low-cost and easy processing.[28] Among these, PAA was used as it has the potential to remove dyes and metal ions from polluted water and overcome antibacterial activities due to the carboxylic group (COOH).[29]

Carbon-based materials like amorphous carbon, graphitized carbon, nanotubes, and graphene are extensively used as matrix materials with the advantages of flexibility, chemical stability, and structural heterogeneity.[30] Graphene oxide (GO) is a 2D aromatic compound with a hexagonal lattice of sp^2 carbon atoms with a long-range π-conjugation bond and a monolayer structure with oxygen functional groups, bearing on the basal planes and edges of GO sheets. GO is introduced to increase the concentration of charge carriers in SnO_2 by increasing conductivity[31] and a larger surface area. This work synthesized pristine SnO_2 and doped it with different concentrations of GO and a fixed amount of PAA *via* co-precipitation methodology. The catalytic efficiency of the prepared samples was examined to remove the synthetic methylene blue (MB) dye, and bactericidal activity was investigated against *E. coli* by the agar well diffusion method. Molecular docking predictions were performed against enzymes selected from the cell wall and nucleic acid synthesis pathways, i.e., beta-lactamase$_{E.\ coli}$ and DNA gyrase$_{E.\ coli}$, respectively.

2. EXPERIMENTAL WORK

2.1. Chemicals. Tin chloride dihydrate ($SnCl_2{\cdot}2H_2O$, 99%), NaOH (99%), poly[acrylic acid ($C_3H_4O_2$)]$_n$, graphite powder (99.5%), sodium nitrate ($NaNO_3$), potassium permanganate ($KMnO_4$, 99.5%), hydrogen peroxide (H_2O_2), and 2, 2-diphenyl-1-picryl-hydrazyl-hydrate (DPPH) were purchased from Sigma-Aldrich (Germany). Sulfuric acid (H_2SO_4) and hydrochloric acid (HCl) were procured from Analar.

2.2. Synthesis of Graphene Oxide. For the synthesis of GO, a modified Hummer's route was adopted.[32] First, 2 g of graphite powder and 1 g of $NaNO_3$ were dissolved in 46 mL of concentrated H_2SO_4 in an ice bath and stirred for 10 min. $KMnO_4$ was introduced at >5 °C, turning the solution color from purple to yellow at magnetic stirring on an ice bath for 24 h. Further, 12 mL H_2O_2 was incorporated, and the solution was centrifuged at 7000 rpm for 7 min and washed with HCl and deionized (DI) water to obtain a residue. The accumulation was heated for 12 h to receive a powder that was converted into a fine powder by grinding, as shown in Figure 1a.

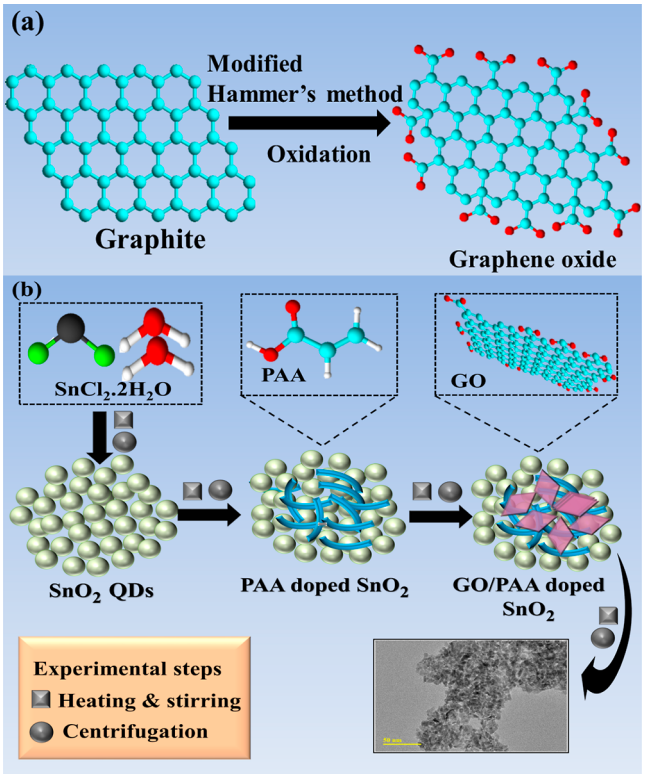

Figure 1. (a) Schematic illustration of GO and (b) synthesis of pristine and doped SnO_2.

2.3. Synthesis of GO/PAA-Doped SnO_2. To synthesize SnO_2 quantum dots (QDs), 0.5 M of $SnCl_2{\cdot}2H_2O$ was prepared under constant magnetic stirring at 80 °C by the co-precipitation method. 1 M solution of precipitating agent NaOH was added in the above solution drop-by-drop to retain pH ∼10, and the precipitate formed. Subsequently, the colloidal solution was centrifuged at 7000 rpm repeatedly for 8 min to collect the precipitates. The sediments were heated overnight at 90 °C to obtain nanopowders and later crushed into a fine powder. Similarly, various concentrations of GO (50 and 100 mg) and a fixed amount of PAA (6 wt %)-doped SnO_2 QDs were prepared, as demonstrated in Figure 1b.

2.4. Isolation and Identification of *E. coli*. *2.4.1. Sample Collection.* Samples from the selected breastfeeding cows are sucked up directly into sterile glassware and supplied at various markets, veterinary centers, and farms in Punjab, Pakistan. After being collected at 4 °C, raw milk was immediately brought to the lab. On MacConkey agar, pathogens in raw milk were collected. For 48 h, all plates were cultured at 37 °C.

2.4.2. Identification and Characterization of Bacterial Isolates. According to Bergey's Manual of Determinative Bacteriology, the primary detection of *E. coli* is based on the Gram stain of colonial morphology and different biochemical tests.[33]

2.4.3. Antibiotic Susceptibility. Mueller Hinton agar (MHA) utilized for the disc diffusion method of Bauer *et al.*[34] to perform the antimicrobial sensitivity test. The test was performed to find out whether *E. coli* was resistant to the following antibiotics (classes): Ceftriaxone (Cro) 30 μg (Cephalosporins), Gentamicin (Gm) 10 μg (Aminoglycosides), Ciprofloxacin (Cip) 5 μg (Quinolones), Tetracycline (Te) 30 μg (Tetracyclines), Imipenem (Imi) 10 μg (Carbapenem), Amoxycillin (A) 30 μg (Penicillins), and

https://doi.org/10.1021/acsomega.2c07460
ACS Omega 2023, 8, 5808−5819

Azithromycin (Azm) 15 μg (Macrolides).[35] From these antibiotics, Ciprofloxacin (Cip) 5 μg (Quinolones) was adopted for the antibacterial activity of synthesized GO/PAA-SnO_2. *E. coli*-purified cultures developed and balanced 0.5 MacFarland turbidity. After that, it was spread-plated on Muller Hinton Agar (MHA) (Oxoid Limited, Basingstoke, UK). The antibiotic discs were kept from the infected plate to prevent the intersection of inhibition zones. The results were interpreted following the Clinical and Laboratory Standard Institute[36] when plates were incubated at 37 °C for 24 h. A bacterium is an MDR if it is robust to at least three antibiotics.[37]

2.4.4. Antimicrobial Activity. The antimicrobial sensitivity of pure and doped SnO_2 nanoparticles was analyzed by the agar well diffusion method for 10 characteristic isolates of *E. coli* taken from mastitic milk. *E. coli* at 1.5 108 CFU/mL (0.5 McFarland standard) was swabbed onto MacConkey agar in Petri plates. Employing a sterile cork borer, 6 mm diameter wells were created. Various concentrations of GO/PAA-SnO_2 incorporated with the prepared well as maximum and minimum doses. A positive control of ciprofloxacin and a negative control of DIW were utilized.[38]

2.4.5. Statistical Analysis. The inhibition region diameters were statistically evaluated using one-way analysis of variance (ANOVA) in SPSS 20 to access the antibacterial activity measured for the inhibition zone size (mm).[39]

2.5. Molecular Docking Studies. The role of molecular docking studies in revealing mysteries behind numerous biological activities has gained considerable attention over the last few decades. Using computational tools to predict the possible part of a given molecule has made novel drug discovery more feasible and cost effective. Inhibitors of enzymes essential for bacterial growth lead to the discovery of new drug candidates, specifically those belonging to cell wall synthesis and nucleic acid syntheses like beta-lactamase and DNA gyrase.[40−42] Here, we evaluated the binding capacity of the given nanocomposites, i.e., SnO_2, PAA-SnO_2, and GO/PAA-SnO_2, against these enzyme targets. Molecular docking calculations were conducted using ICM Molsoft software.[39] 3D structural coordinates of enzymes selected as possible targets were obtained from the protein data bank. The PDB IDs used for beta-lactamase and DNA gyrase were 4KZ9 (Res: 1.7 Å)[43] and 5MMN (Res: 1.9 Å),[44] respectively. The energy minimization of enzyme structures was done using the MMFF94x force field and gradient: 0.05 while the binding pocket was specified (within 5 Å of native ligand) to obtain a detailed view of the interaction pattern of the given nanocomposites inside the active pocket.

The standard protocol of ICM Molsoft was used for protein structure preparation involving the elimination of water molecules and native ligands, accumulation of gastegier charges, and polar H-atoms. The best-docked complexes were generated in each case for an in-depth analysis (i.e. 10 top-ranked docked conformations). Finally, the 3D-viewer of ICM Molsoft was used for the graphical representation of interaction patterns. The ligand structures were prepared using the Chemdraw and ligedit tool of ICM and the most stable conformation was produced for every ligand using the conformational analysis tool.

2.6. Catalytic Activity. The catalytic activity (CA) of GO/PAA-SnO_2 was determined in the presence of $NaBH_4$ to decolorize the MB. First, 3 mL aqueous solution of MB was mixed with a synthesized (400 μL) solution of $NaBH_4$ and after regular intervals, the absorption rate was calculated. Subsequently, 400 μL of pure and GOPAA-SnO_2 was added as a catalyst under vigorous stirring, and the decolorization of dye occurred as a result of the redox reaction. By a UV−vis spectrophotometer, degradation efficiency was examined, and maximum wavelength (λ_{max}) for MB was achieved at 665 nm for all samples. The CA was calculated by using the % degradation formula given as

$$\%\ \text{degradation} = \frac{C_o - C_t}{C_o} \times 100$$

where C_o represents the initial value of dye and C_t shows the time-dependent concentration.

2.6.1. Catalytic Mechanism. $NaBH_4$ acts as a reducing agent for the catalytic reduction and donates an electron to the redox reduction. MB is a positive dye that receives an electron as an oxidizing agent. Redox reaction occurs during CA when an electron transfers from a reducing agent to an oxidizing agent. The electron is absorbed by MB and causes the degradation of synthetic dye. Eventually, MB dye was evaluated in the presence of $NaBH_4$, which was time consuming and slow. To solve this issue, the addition of the nanocatalyst (GO/PAA-SnO_2) into the oxidation−reduction reaction provides electrons and transferred electrons from BH^-_4 to MB dye and as a result, MB was reduced into LMB (Figure 2).

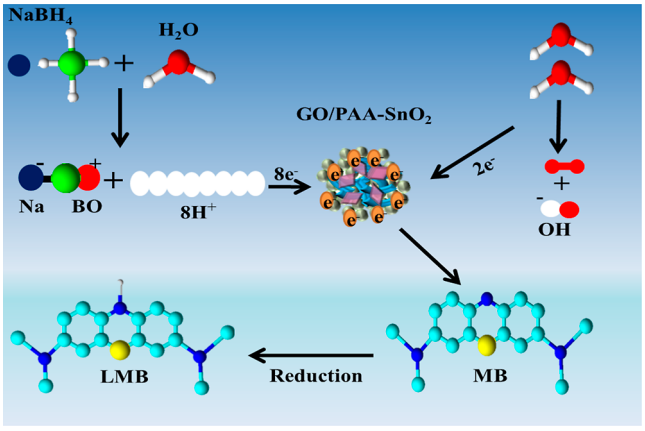

Figure 2. Schematic illustration of catalysis of doped SnO_2.

2.7. Radical Scavenging Assay. To analyze free radical active species and anti-oxidant activity of nanocomposites, a modified version of the DPPH scavenging experiment was adopted. GO/PAA-doped SnO_2 nanoparticles (50−250 μg/mL) were mixed with an equal volume of (0.1 mM) DPPH solution. This mixture was vortexed and incubated for 30 min at room temperature in the dark. A standard solution of ascorbic acid was employed as a reference sample. The degradation of DPPH solution (λ = 517 nm) was employed to calculate the scavenging rate (%) of each sample by eq 1

$$\text{scavenging rate}\ (\%) = A_0 - A_1/A_0 \times 100 \quad (1)$$

A_0 and A_1 = control absorbance and standard absorbance.

3. RESULTS AND DISCUSSION

X-ray diffraction (XRD) analysis was employed in the 2θ range from 20 to 60° to investigate the crystal structure, phase constitution, and crystallinity of pristine and GO/PAA-SnO_2,

https://doi.org/10.1021/acsomega.2c07460
ACS Omega 2023, 8, 5808−5819

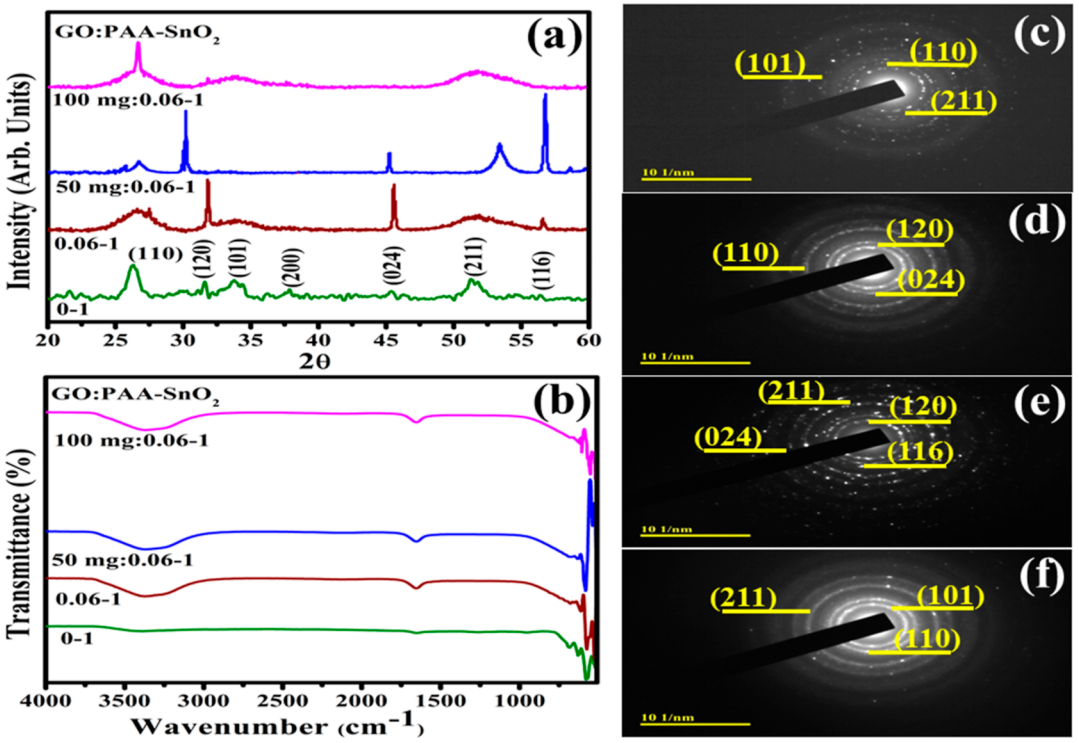

Figure 3. XRD patterns (a), Fourier transform infrared (FTIR) spectra (b), and SAED patterns (c–f) of SnO_2 and GO/PAA-SnO_2.

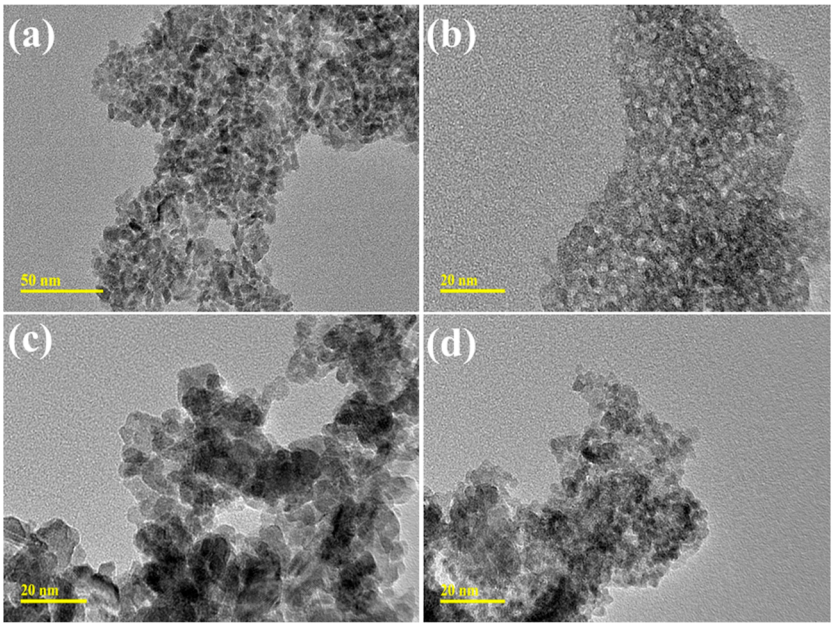

Figure 4. (a–d) Transmission electron microscopy (TEM) morphology of synthesized SnO_2 and GO/PAA-SnO_2.

as illustrated in Figure 3a. The observed diffraction peaks sited at 26.4° (110), 33.8° (101), 37.7° (200), 51.36° (211), and 56.4° (116) were attributed to the tetragonal structure of SnO_2 (JCPDS card 00-041-1445) along with the *P*42/*mm* space group.[45] Additional peaks detected at 30.1° (020) and 45.4° (024) correspond to the anorthic structure of SnO (JCPDS no. 01-085-0423).[46] The broadness of peaks observed upon the incorporation of PAA might be associated with its amorphous nature.[26] It is noteworthy that peak intensity increased with a low concentration of GO to PAA/SnO_2 relative to a higher concentration of GO attributed to the anchoring of QDs on GO sheets.[47] The shifting of peaks toward lower angles upon doping represented the incorporation of functionalized GO on SnO_2 QDs.[48] The trend was reversed upon the higher concentration of GO due to the formation of oxygen-containing functional groups, including hydroxyl, epoxy, and carboxyl, that might have enhanced the interlayer distance.[49]

To elucidate the existence of a functional group present in the product as pristine and doped SnO_2, the Fourier transform infrared (FTIR) technique was employed, as elaborated in Figure 3b. Transmittance bands at 3662 and 1650 cm^{-1} can be attributed to O–H vibrations.[50] The band at 625 cm^{-1} is due

https://doi.org/10.1021/acsomega.2c07460
ACS Omega 2023, 8, 5808–5819

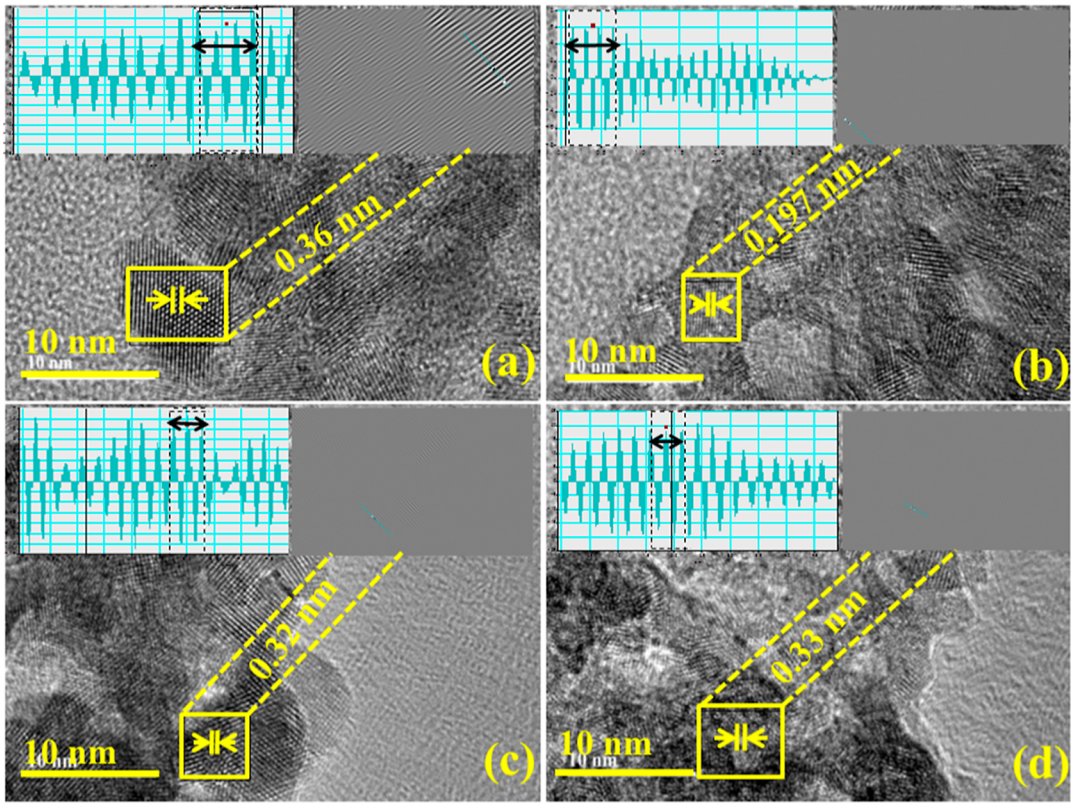

Figure 5. (a–d): d-spacing of SnO_2 and PAA-SnO_2, 50 and 100 mg GO/PAA-SnO_2, respectively.

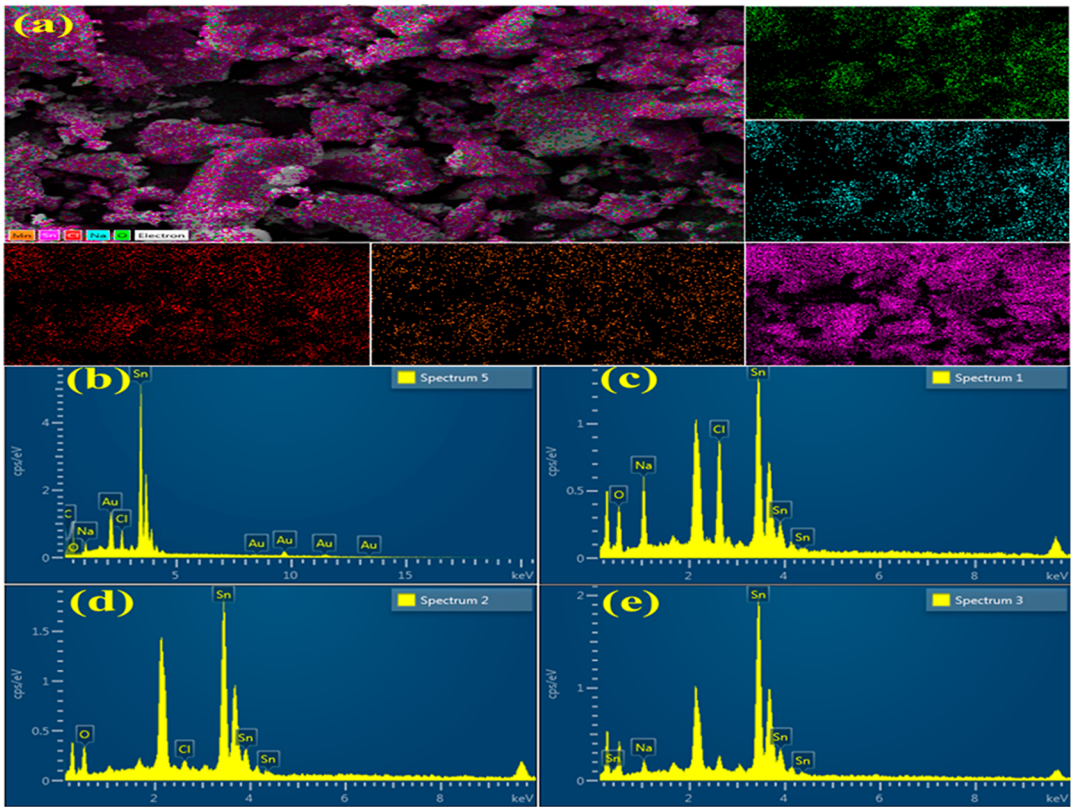

Figure 6. (a) Mapping of all components distribution, EDS image of SnO_2 (b), PAA-SnO_2 (c), 50 mg GO/PAA-SnO_2 (d), and 100 mg GO/PAA-SnO_2 (e).

to SnO_2 framework vibrations in the doped SnO_2,[51] and peaks at 681 and 572 cm^{-1} are assigned to Sn−O−Sn stretching and bending modes of SnO_2, respectively.[52,53] Upon the addition of PAA, the bands shifted toward a higher wave number of

https://doi.org/10.1021/acsomega.2c07460
ACS Omega 2023, 8, 5808−5819

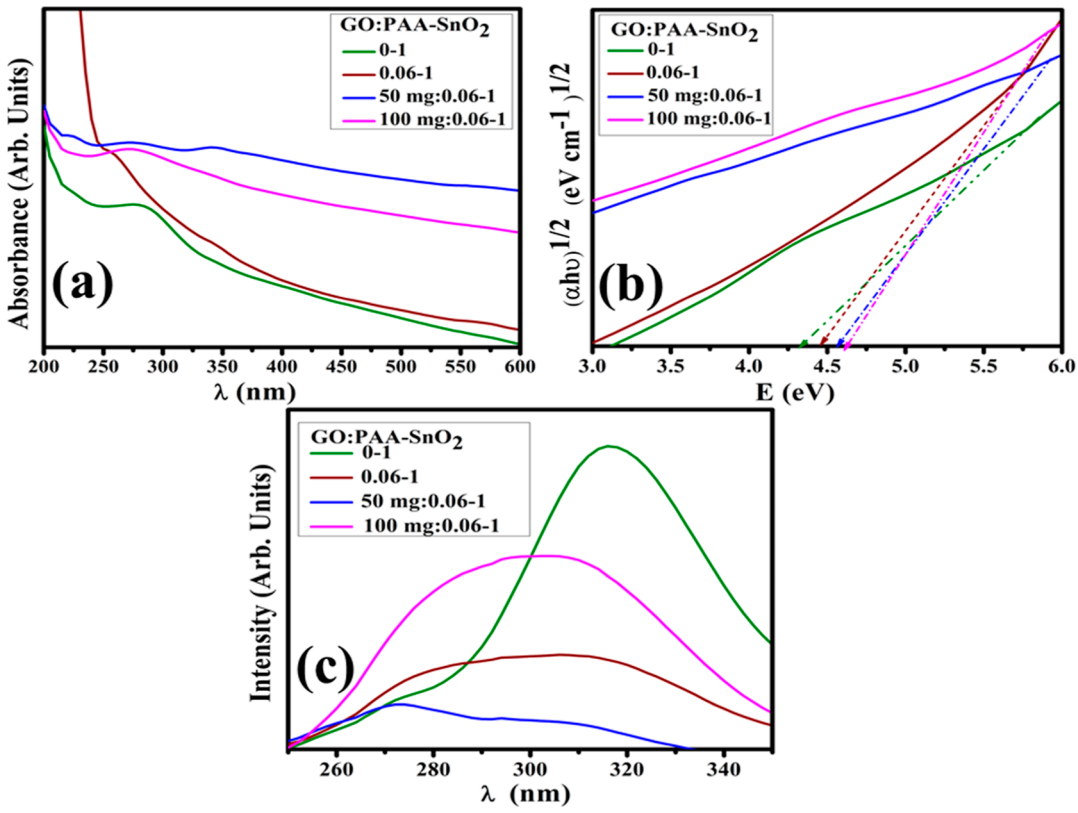

Figure 7. (a) Absorption spectra, (b) band gap energy plot, and (c) photoluminescence spectra.

~3700−3000 cm^{-1}, ascribed to the occurrence of absorbed water molecule and O−H group.[53] There was no notable shift in spectra by the incorporation of GO. Selected area electron diffraction (SAED) analysis indicates the bright circular rings of pristine and GO/PAA-SnO_2 exhibited the high crystalline nature of samples. The corresponding planes (110), (211), (101), and (120) are well correlated with XRD results (Figure 3c−f).

The morphologies of SnO_2 and doped SnO_2 were examined by transmission electron microscopy (TEM) analysis (Figure 4a−d). TEM micrographs confirmed the formation of agglomerated QDs of SnO_2;[54] this agglomeration could be due to hydrogen bonding of DI water during the synthesizing process (Figure 4a). Upon doping of the capping agent (PAA), a higher degree of agglomerations was observed with a reduction in the particle size confirmed through image J software (Figure 4b). The incorporation of GO (50 mg) into PAA/SnO_2 showed overlapping of GO nanosheets around QDs (Figure 4c) and the same trend was noted with a higher concentration of GO (100 mg), as illustrated in Figure 5d. The particle sizes of 8 and 6 nm were calculated through image J software of SnO_2 and PAA-SnO_2, respectively (Figure 5c,d). The measured d-spacing values of SnO_2 and doped SnO_2 were 0.27, 0.17, 0.19, and 0.26 nm, which are well harmonized with XRD analysis (Figure 5a−d).

Energy-dispersive spectroscopy (EDS) analysis was performed to identify the elemental composition of SnO_2 and doped SnO_2 (Figure 6b−e). Sn and O peaks were observed that confirm the formation of SnO_2. The Na and Cl peaks were detected due to precipitating agent NaOH during the synthesis of samples for pH control. The Au peak originated during the coating sputtered on the samples to lessen the charging effect. The elemental mapping of the prepared samples (Figure 6a) confirms the presence of Sn and O.

To examine the optical properties of synthesized QDs, electronic spectroscopy was utilized in a wavelength range of 200−600 nm (Figure 7a). Spectra revealed a strong absorption peak at 284 nm for SnO_2[55] corresponding to the $\pi-\pi^*$electronic transition.[56] Tauc's equation determined the band gap energy (E_g), and indirect E_g was calculated at 4.4 eV for SnO_2 (Figure 7b). After doping, E_g increased from 4.4 to 4.75 eV, indicating the functionalization of GO nanosheets on smaller QDs.[57] This increase in E_g upon doping confirmed the reduction in the crystallite size.

PL spectroscopy was employed to determine the electron−hole recombination rate and charge-transfer capability of bare and doped SnO_2 (Figure 7c). The emission peak of SnO_2 was noted at 314 nm,[58] which is attributed to fluorescence phenomena. Peak intensity was reduced by adding PAA to SnO_2, indicating a low recombination rate and introducing a blue shift. The PL intensity of PAA-SnO_2 is significantly lower than that of SnO_2 QDs, indicating that charge transfer occurs efficiently in the PAA-SnO_2. The PL results showed that SnO_2 dispersed uniformly and that PAA conjugation effectively suppressed electron−hole pair recombination in the prepared sample.[59] The addition of GO to PAA/SnO_2 decreased the peak intensity gradually, with higher concentrations ascribed to phosphorescence phenomena.[60]

A UV−vis spectrophotometer investigated the CA of control and GO/PAA-SnO_2. Degradation efficiency for MB was calculated in the presence of reducing agent $NaBH_4$ and prepared samples that acted as a catalyst in a redox reaction. An electrochemical mechanism can explain the catalytic process, in which GO/PAA-SnO_2 acts as an electron relay for the oxidant and reductant and electron transfer occurs *via*

https://doi.org/10.1021/acsomega.2c07460
ACS Omega 2023, 8, 5808−5819

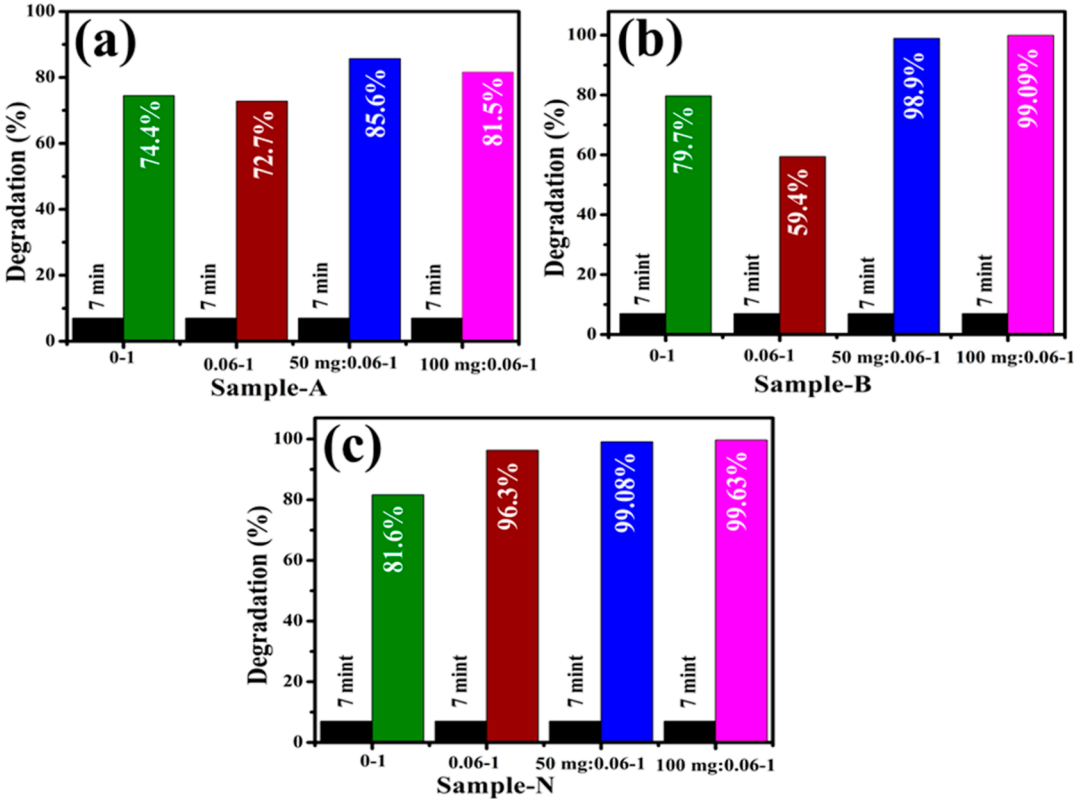

Figure 8. Catalytic dye degradation (%) GO/PAA-SnO_2 in (a) acidic, (b) basic, and (c) neutral media.

the metal nanoparticles.[61] Catalytic activity is dependent on the catalyst concentration because it enhances dye degradation by lowering the activation energy of a chemical reaction. In general, larger surface area catalysts have demonstrated a higher catalytic performance because they contain more active sites and the pH of the solution has a significant impact on the degradation efficiency.[54] Due to the possibility of a large redox potential difference between the electron donors and acceptor species, which can inhibit electron transfer, the electron-transfer step plays a dynamic role in dye degradation.[62] The bond dissociation energy is important during chemical reactions as it breaks and/or generates new bonds. Electron transfer occurs during the reaction in which $NaBH_4$ acts as a donor and the dye as an acceptor.[63] The addition of SnO_2 nanocatalysts to the reaction mixture acted as a potential intermediate between MB dye and BH_4 ions. Dye degradation for 7 min was measured to be 74.4, 72.7, 85.6, and 81.5% in an acidic medium; 79.9, 59.4, 98.9, and 99.09% in a basic medium; and 81.6, 96.3, 99.0, and 99.63% in a neutral medium (Figure 8a–c). The absorption spectra of GO/PAA-SnO_2 in the neutral medium have been provided in the supplementary file (Figure S1). The highest catalytic activity was exhibited by 100 mg (GO) doped PAA/SnO_2 in basic and neutral media, while in an acidic medium, 50 mg (GO) showed the maximum effect of degradation. Incorporation of PAA provides carboxylic groups, and more carboxyl groups can provide more active absorption sites to remove the dyes.[64] CA performance is substantially affected by the crystallite size, surface area, and shape of nanocatalysts and combination of 2D materials and quantum dots. This elevated efficiency was attributed to more active sites offered by the large surface area of the nanocatalyst. Moreover, a tiny variation between neutral and basic media is ascribed to the enhanced electrostatic attraction between MB^+, a positively charged dye, and the negatively charged catalyst. The nanocatalyst surface in the basic medium tends to acquire a negative charge, while the absorption of cationic adsorbate species in acidic media is hindered by the positively charged surfaces of catalysts.[65] The charge on the catalyst surface developed gradually became negative as pH was raised, boosting the adsorption ability of cationic dyes on SnO_2 and GO/PAA-SnO_2 nanocatalysts.

The bactericidal potential of pure and doped SnO_2 was evaluated through an agar well diffusion approach. *E. coli* bacteria extracted from caprine or bovine mastitic milk. For synthesized samples, inhibition regions of *E. coli* (Gram −ve bacteria) were revealed to be 0.35−2.95 mm and 1.75−3.45 mm for the corresponding lower (0.5 mg/50 μL) and higher (1.0 mg/50 μL) doses. Positive control ciprofloxacin indicated 5.35 mm inhibitory domains against *E. coli* compared to the negative control DI water 0 mm, as listed in Table 1.

The antibacterial activity has an inverse relation with the size of the material. Small-sized NPs produced reactive oxygen species (ROS) that are effectively influenced by Gram-negative bacteria with an extra outer membrane. Nanomaterials destroy

Table 1. Measurement of Inhibition Zone (mm)

	E. coli inhibition zone (mm)	
GO/PAA-SnO_2	0.5 mg/50 μL	1.0 mg/50 μL
0−1	0.35	1.75
0.06−1	1.90	2.75
50 mg: 0.06−1	2.45	3.10
100 mg: 0.06−1	2.95	3.45
ciprofloxacin	5.35	5.35
DI water	0	0

https://doi.org/10.1021/acsomega.2c07460
ACS Omega 2023, 8, 5808−5819

the micro-organisms by attacking the cell wall/membrane, destroy DNA to stop the production of cells, and produce ROS, such as hydrogen peroxide (H_2O_2), radicals (OH^-), and anions (O_2^-), which ultimately results in cell death. Electrostatic interface, membrane deformation, cytoplasmic material leakage, DNA breakage, and protein denaturation induced by the positively charged NP surface acting as an antibacterial agent toward the highly reactive negatively charged bacterial cell membrane are[66] shown in Figure 9.

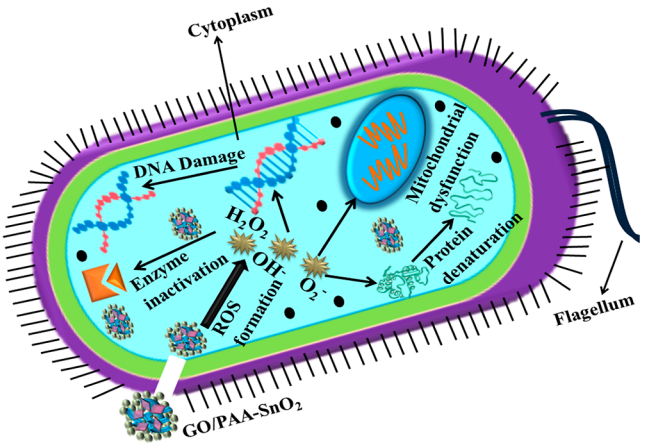

Figure 9. Bactericidal mechanism of prepared samples.

Molecular docking studies of synthesized nanomaterials revealed their possible interactions with active site residues of given enzyme targets. These nanocomposites demonstrated moderate binding energies against beta-lactamase$_{E.\ coli}$ showing their critical interaction with key amino acids. Docked complexes obtained for PAA-SnO_2 and GO/PAA-SnO_2 showed H-bonds with Arg232 (2.8 Å; 2.5 Å) and Lys183 (2.1 Å; 2.0 Å) having binding scores −6.928 and −7.223 kcal/mol, respectively, as depicted in Figure 10b,c. Similarly, pristine SnO_2 also formed a stable docked complex (binding score −4.675 kcal/mol) with beta-lactamase$_{E.\ coli}$ showing H-bond interactions with Thr226 (2.2 Å), suggesting its possible role as an inhibitor for beta-lactamase (Figure 10a).

In the case of DNA gyrase$_{E.\ coli}$, almost similar binding trends were shown by synthesized nanocomposites where pristine SnO_2 showed single H-bonds (2.1 Å) with Thr165 amino acid of active pocket alongside metal-contact interactions with Asp73 with an overall binding score of −5.771 kcal/mol, as shown in Figure 11a. On the other hand, PAA-SnO_2 showed a more stable docked complex having three H-bonds within the active site, i.e., Asp73 (2.9 Å), Arg136 (2.4 Å), and Thr165 (2.0 Å) with a binding score of −8.552 kcal/mol. Similarly, the GO/PAA-SnO_2 docked complex involved two amino acid residues of active pocket, i.e., Thr165 (H-bond: 2.2 Å) and Asp73 (metal-contact interaction) having a binding score of −4.461 kcal/mol, as depicted in Figure 11b,c.

In silico molecular docking studies are comparable to *in vitro* bactericidal activity against *E. coli* and suggested pristine SnO_2

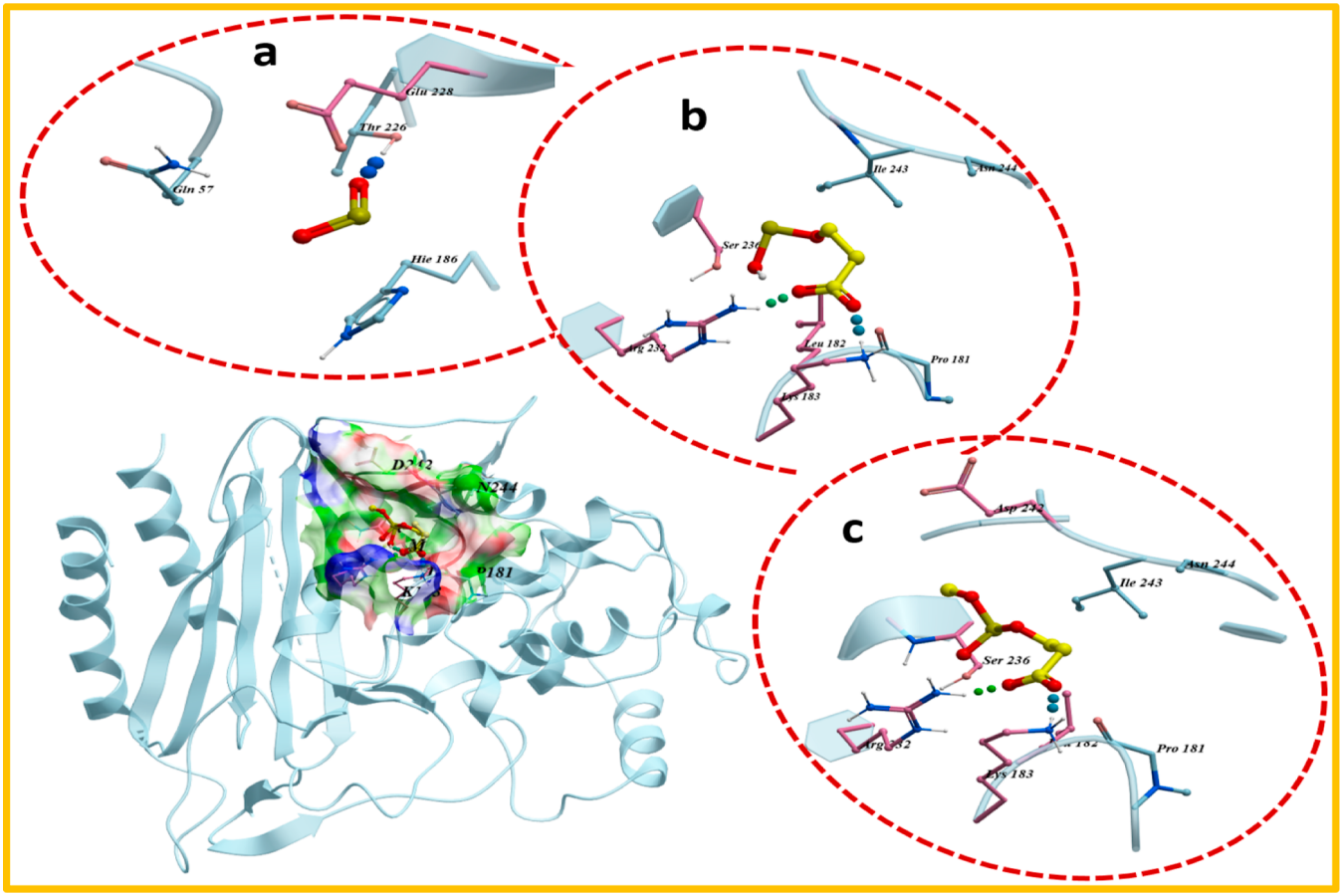

Figure 10. 3D view of binding interaction of nanocomposites within active sites of beta-lactamase$_{E.\ coli}$ (a) SnO_2, (b) PAA-SnO_2, and (c) GO/PAA-SnO_2.

https://doi.org/10.1021/acsomega.2c07460
ACS Omega 2023, 8, 5808−5819

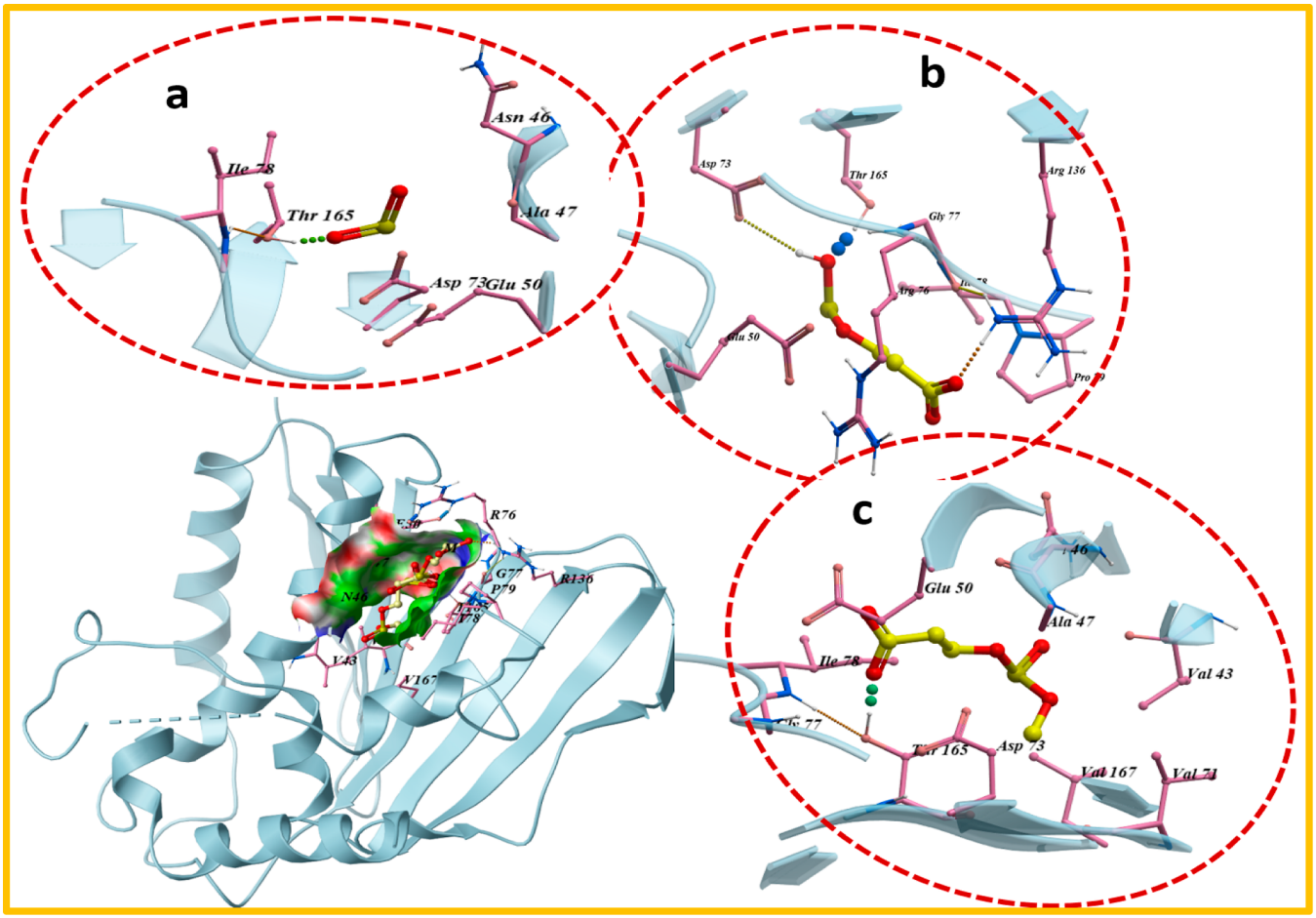

Figure 11. 3D view of binding interaction of nanocomposites within the active site of DNA gyrase$_{E.\ coli}$ (a) SnO_2, (b) PAA-SnO_2, and (c) GO/PAA-SnO_2.

and its composites with PAA and GO/PAA as potential inhibitors of beta-lactamase and DNA gyrase that needs to be explored further.

DPPH scavenging assay was developed to investigate and quantify anti-oxidant effects of active radical species (Figure 12). Antioxidant properties of compounds are inter-related with their tendency to transfer hydrogen or electron atoms to DPPH free radicals, resulting in stable diamagnetic compounds. All prepared samples displayed a dose-dependent anti-oxidant potential. GO/PAA-SnO_2 (100 mg: 0.06−1) exhibited highest scavenging performance of up to 53.45% at a 250 μg/mL concentration and scavenged DPPH radicals. The formation of highly reactive $^{\bullet}OH$ and $^{\bullet}O_2$ radical species can interact with DPPH free radicals and results in its degradation,[67] which is highly correlated with the standard (ascorbic acid).

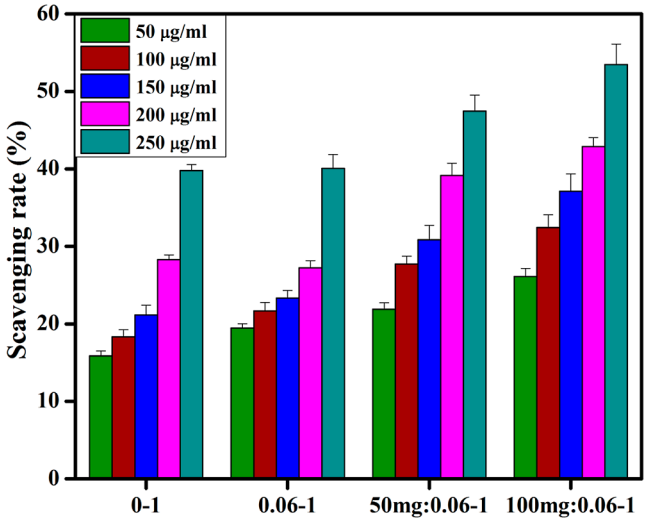

Figure 12. Scavenging potential of synthesized nanocomposites.

In order to facilitate electron transport, bacteria used a class of chemicals called redox mediators. Similarly to oxidation−reduction reactions, degradation of dyes proceeds. The greatest deterioration was seen when a redox mediator was used.[68] The rate-limiting phase in the anaerobic dye reduction process has been proven to involve the transfer of reducing equivalents from the main electron donor (like co-substrate) to the terminal electron acceptor.[69] In order to hasten the electron-transfer phase while decreasing steric hindrance from dye molecules, a little amount of redox mediator supplementation is necessary.[19,70]

4. CONCLUSIONS

In this study, we successfully synthesized the QDs of SnO_2 doped with varying GO concentrations (50 and 100 mg) with a fixed amount of PAA (6 wt %) for bactericidal and catalytic efficiencies *via* the co-precipitation technique. XRD analysis

https://doi.org/10.1021/acsomega.2c07460
ACS Omega 2023, 8, 5808−5819

confirmed the tetragonal structure of SnO_2. The decrease in absorption was observed upon doping accompanied by a blue shift, and band gap energy was increased from 4.3 to 4.75 nm. The formation of SnO_2 QDs was confirmed by HR-TEM analysis. The FTIR peak at 6250 cm^{-1} confirmed the presence of SnO_2 through Sn−O stretching vibrations. The pristine and co-doped SnO_2 showed excellent catalytic activity against MB dyes in all media (81.5, 99.09, and 99.63%). Pure SnO_2 and GO/PAA-SnO_2 demonstrated good catalytic and antibacterial potency for removing dyes and pathogens from wastewater, respectively. *In silico* predictions agreed with antibacterial activities against *E. coli* and suggested the given nanocomposites as possible inhibitors of beta-lactamase and DNA gyrase.

■ ASSOCIATED CONTENT

Supporting Information

The Supporting Information is available free of charge at https://pubs.acs.org/doi/10.1021/acsomega.2c07460.

Absorption graph of GO/PAA-SnO_2 for degradation of MB dye (PDF)

■ AUTHOR INFORMATION

Corresponding Authors

Muhammad Ikram − *Solar Cell Applications Research Lab, Department of Physics, Government College University Lahore, Lahore 54000 Punjab, Pakistan;* orcid.org/0000-0001-7741-789X; Email: dr.muhammadikram@gcu.edu.pk

Walid Nabgan − *DepartamentdʼEnginyeriaQuímica, UniversitatRovira i Virgili, Tarragona 43007, Spain*; Email: wnabgan@gmail.com

Ali Al-Shanini − *College of Petroleum and Engineering, Hadhramout University, Mukalla, Hadhramout, Yemen;* orcid.org/0000-0002-7616-7814; Email: a.alshanini@hu.edu.ye

Authors

Saira Riaz − *Solar Cell Applications Research Lab, Department of Physics, Government College University Lahore, Lahore 54000 Punjab, Pakistan*

Sadia Naz − *Tianjin Institute of Industrial Biotechnology, Chinese Academy of Sciences, Tianjin 300308, China*

Anum Shahzadi − *Faculty of Pharmacy, The University of Lahore, Lahore 54000, Pakistan*

Anwar Ul-Hamid − *Core Research Facilities, King Fahd University of Petroleum & Minerals, Dhahran 31261, Saudi Arabia;* orcid.org/0000-0002-0259-301X

Ali Haider − *Department of Clinical Sciences, Faculty of Veterinary and Animal Sciences, Muhammad Nawaz Shareef, University of Agriculture, Multan 66000 Punjab, Pakistan*

Junaid Haider − *Tianjin Institute of Industrial Biotechnology, Chinese Academy of Sciences, Tianjin 300308, China;* orcid.org/0000-0002-2254-1196

Complete contact information is available at: https://pubs.acs.org/10.1021/acsomega.2c07460

Notes

The authors declare no competing financial interest.
Availability of data: data available on demand.

■ ACKNOWLEDGMENTS

The authors thank higher education commission (HEC), Pakistan, for financial support through NRPU 20-17615 (Dr. Muhammad Ikram).

■ REFERENCES

(1) Wang, Z.; Wu, A.; Colombi Ciacchi, L. C.; Wei, G. Recent Advances in Nanoporous Membranes for Water Purification. *Nanomaterials* **2018**, *8*, 65.

(2) Shaheen, S.; Iqbal, A.; Ikram, M.; Ul-Ain, K.; Naz, S.; Ul-Hamid, A.; Shahzadi, A.; Haider, A.; Nabgan, W.; Haider, J. Effective Disposal of Methylene Blue and Bactericidal Benefits of Using GO-Doped MnO2Nanorods Synthesized through One-Pot Synthesis. *ACS Omega* **2021**, *6*, 24866−24878.

(3) Zhang, J. The Impact of Water Quality on Health: Evidence from the Drinking Water Infrastructure Program in Rural China. *J. Health Econ.* **2012**, *31*, 122−134.

(4) Shaban, M.; Ashraf, A. M.; Abukhadra, M. R. TiO2 Nanoribbons/Carbon Nanotubes Composite with Enhanced Photocatalytic Activity; Fabrication, Characterization, and Application. *Sci. Rep.* **2018**, *8*, 781.

(5) Rafiq, A.; Imran, M.; Aqeel, M.; Naz, M.; Ikram, M.; Ali, S. Study of Transition Metal Ion Doped CdS Nanoparticles for Removal of Dye from Textile Wastewater. *J. Inorg. Organomet. Polym. Mater.* **2020**, *30*, 1915−1923.

(6) Kausar, A.; Iqbal, M.; Javed, A.; Aftab, K.; Nazli, Z. i. H.; Bhatti, H. N.; Nouren, S. Dyes Adsorption Using Clay and Modified Clay: A Review. *J. Mol. Liq.* **2018**, *256*, 395−407.

(7) Mahanthappa, M.; Kottam, N.; Yellappa, S. Enhanced Photocatalytic Degradation of Methylene Blue Dye Using CuS−CdS Nanocomposite under Visible Light Irradiation. *Appl. Surf. Sci.* **2019**, *475*, 828−838.

(8) Lops, C.; Ancona, A.; Di Cesare, K.; Dumontel, B.; Garino, N.; Canavese, G.; Hérnandez, S.; Cauda, V. Sonophotocatalytic Degradation Mechanisms of Rhodamine B Dye via Radicals Generation by Micro- and Nano-Particles of ZnO. *Appl. Catal. B Environ.* **2019**, *243*, 629−640.

(9) Neena, D.; Kondamareddy, K. K.; Bin, H.; Lu, D.; Kumar, P.; Dwivedi, R. K.; Pelenovich, V. O.; Zhao, X. Z.; Gao, W.; Fu, D. Enhanced Visible Light Photodegradation Activity of RhB/MB from Aqueous Solution Using Nanosized Novel Fe-Cd Co-Modified ZnO. *Sci. Rep.* **2018**, *8*, 10691.

(10) Hama Aziz, K. H.; Miessner, H.; Mueller, S.; Mahyar, A.; Kalass, D.; Moeller, D.; Khorshid, I.; Rashid, M. A. M. Comparative Study on 2,4-Dichlorophenoxyacetic Acid and 2,4-Dichlorophenol Removal from Aqueous Solutions via Ozonation, Photocatalysis and Non-Thermal Plasma Using a Planar Falling Film Reactor. *J. Hazard. Mater.* **2018**, *343*, 107−115.

(11) Fu, W.; Zhang, W. Microwave-Enhanced Membrane Filtration for Water Treatment. *J. Memb. Sci.* **2018**, *568*, 97−104.

(12) Salimi, F.; Emami, S. S.; Karami, C. Removal of Methylene Blue from Water Solution by Modified Nano-Boehmite with Bismuth. *Inorg. Nano-Metal Chem.* **2018**, *48*, 31−40.

(13) Nasrollahzadeh, M.; Issaabadi, Z.; Sajadi, S. M. Green Synthesis of a Cu/MgO Nanocomposite by: Cassytha Filiformis L. Extract and Investigation of Its Catalytic Activity in the Reduction of Methylene Blue, Congo Red and Nitro Compounds in Aqueous Media. *RSC Adv.* **2018**, *8*, 3723−3735.

(14) Nasrollahzadeh, M.; Sajjadi, M.; Sajadi, S. Biosynthesis of Copper Nanoparticles Supported on Manganese Dioxide Nanoparticles Using Centella Asiatica L. Leaf Extract for the Efficient Catalytic Reduction of Organic Dyes and Nitroarenes. *Cuihua Xuebao/Chinese J. Catal.* **2018**, *39*, 109−117.

(15) Zhang, Y.; Zhai, Y. Preparation of Y-Doped ZrO2 Coatings on MnO2 Electrodes and Their Effect on Electrochemical Performance for MnO2 Electrochemical Supercapacitors. *RSC Adv.* **2016**, *6*, 1750−1759.

(16) Jildeh, Z. B.; Oberländer, J.; Kirchner, P.; Wagner, P. H.; Schöning, M. J. Thermocatalytic Behavior of Manganese (IV) Oxide as Nanoporous Material on the Dissociation of a Gas Mixture Containing Hydrogen Peroxide. *Nanomaterials* **2018**, *8*, 262.
(17) Deng, J.; Ge, Y.; Tan, C.; Wang, H.; Li, Q.; Zhou, S.; Zhang, K. Degradation of Ciprofloxacin Using A-MnO2 Activated Peroxymonosulfate Process: Effect of Water Constituents, Degradation Intermediates and Toxicity Evaluation. *Chem. Eng. J.* **2017**, *330*, 1390−1400.
(18) Mustajab, M.; Ikram, M.; Haider, A.; Ul-Hamid, A.; Nabgan, W.; Haider, J.; Ghaffar, R.; Shahzadi, A.; Ghaffar, A.; Saeed, A. Promising Performance of Polyvinylpyrrolidone-Doped Bismuth Oxyiodide Quantum Dots for Antibacterial and Catalytic Applications. *Appl. Nanosci.* **2022**, *12*, 2621−2633.
(19) Atta, A. H.; El-Shenawy, A. I.; Koura, F. A.; Refat, M. S. Synthesis and Characterization of Some Selenium Nanometric Compounds: Spectroscopic, Biological and Antioxidant Assessments. *World J. Nano Sci. Eng.* **2014**, *04*, 58−69.
(20) Alharbi, N. K.; Alsaloom, A. N. Characterization of Lactic Bacteria Isolated from Raw Milk and Their Antibacterial Activity against Bacteria as the Cause of Clinical Bovine Mastitis. *J. Food Qual.* **2021**, *2021*, 1.
(21) Jensen, K.; Günther, J.; Talbot, R.; Petzl, W.; Zerbe, H.; Schuberth, H. J.; Seyfert, H. M.; Glass, E. J. Escherichia Coli- and Staphylococcus Aureus-Induced Mastitis Differentially Modulate Transcriptional Responses in Neighbouring Uninfected Bovine Mammary Gland Quarters. *BMC Genom.* **2013**, *14*, 36.
(22) Zhang, Y.; Liu, H.; Gao, F.; Tan, X.; Cai, Y.; Hu, B.; Huang, Q.; Fang, M.; Wang, X. Application of MOFs and COFs for Photocatalysis in CO2 Reduction, H2 Generation, and Environmental Treatment. *EnergyChem* **2022**, *4*, 100078.
(23) Liu, X.; Verma, G.; Chen, Z.; Hu, B.; Huang, Q.; Yang, H.; Ma, S.; Wang, X.*Metal-Organic Framework Nanocrystal-Derived Hollow Porous Materials: Synthetic Strategies and Emerging Applications*; The Innovation, 2022.
(24) Yu, S.; Tang, H.; Zhang, D.; Wang, S.; Qiu, M.; Song, G.; Fu, D.; Hu, B.; Wang, X.*MXenes as Emerging Nanomaterials in Water Purification and Environmental Remediation*; Science of the Total Environment, 2022.
(25) Sberveglieri, G.; Concina, I.; Comini, E.; Falasconi, M.; Ferroni, M.; Sberveglieri, V. Synthesis and Integration of Tin Oxide Nanowires into an Electronic Nose. *Vacuum* **2012**, *86*, 532−535.
(26) Jamal, F.; Ikram, M.; Haider, A.; Ul-Hamid, A.; Ijaz, M.; Nabgan, W.; Haider, J.; Shahzadi, I. Facile Synthesis of Silver and Polyacrylic Acid Doped Magnesium Oxide Nanostructure for Photocatalytic Dye Degradation and Bactericidal Behavior. *Appl. Nanosci.* **2022**, *12*, 2409−2419.
(27) He, X.; Dong, W.; Zheng, F.; Fang, L.; Shen, M. Effect of Tartaric Acid on the Microstructure and Photoluminescence of SrTiO3:Pr3+ Phosphors Prepared by a Sol-Gel Method. *Mater. Chem. Phys.* **2010**, *123*, 284−288.
(28) Bhattacharya, S.; Saha, I.; Mukhopadhyay, A.; Chattopadhyay, D.; Chand, U. Role of Nanotechnology in Water Treatment and Purification: Potential Applications and Implications. *Int. J. Chem. Sci. Technol.* **2013**, *3*, 59−64.
(29) Gnecchi, M.; Zhang, Z.; Ni, A.; Dzau, V. J. Paracrine Mechanisms in Adult Stem Cell Signaling and Therapy. *Circ. Res.* **2008**, *103*, 1204−1219.
(30) Wang, F.; Cheng, T.; Zong, J.; Zhao, M.; Yang, S.; Song, X. SnO2/Graphene Nanocomposite Coated by Carbonized Polyacrylic Acid Hydrogel as a High-Performance Anode for Lithium-Ion Batteries. *ChemistrySelect* **2019**, *4*, 8082−8088.
(31) Wang, Y.; Djerdj, I.; Smarsly, B.; Antonietti, M. Antimony-Doped Sno2 Nanopowders with High Crystallinity for Lithium-Ion Battery Electrode. *Chem. Mater.* **2009**, *21*, 3202−3209.
(32) Qumar, U.; Hassan, J.; Naz, S.; Haider, A.; Raza, A.; Ul-Hamid, A.; Haider, J.; Shahzadi, I.; Ahmad, I.; Ikram, M. Silver Decorated 2D Nanosheets of GO and MoS2serve as Nanocatalyst for Water Treatment and Antimicrobial Applications as Ascertained with Molecular Docking Evaluation. *Nanotechnology* **2021**, *32*, 255704.
(33) Sinclair, C. G. Bergey's Manual of Determinative Bacteriology. *Am. J. Trop. Med. Hyg.* **1939**, *s1-19*, 605−606.
(34) Bauer, A. W.; Kirby, W. M.; Sherris, J. C.; Turck, M. Antibiotic Susceptibility Testing by a Standardized Single Disk Method. *Am. J. Clin. Pathol.* **1966**, *45*, 493−496.
(35) Adzitey, F.; Yussif, S.; Ayamga, R.; Zuberu, S.; Addy, F.; Adu-Bonsu, G.; Huda, N.; Kobun, R. Antimicrobial Susceptibility and Molecular Characterization of Escherichia Coli Recovered from Milk and Related Samples. *Microorganisms* **2022**, *10*, 1335.
(36) Richter, S. S.; Ferraro, M. J.Susceptibility Testing Instrumentation and Computerized Expert Systems for Data Analysis and Interpretation. In *Manual of Clinical Microbiology*; Wiley, 2011; pp 1144−1154.
(37) Iwalokun, B. A.; Ogunledun, A.; Ogbolu, D. O.; Bamiro, S. B.; Jimi-Omojola, J. In Vitro Antimicrobial Properties of Aqueous Garlic Extract against Multidrug-Resistant Bacteria and Candida Species from Nigeria. *J. Med. Food* **2004**, *7*, 327−333.
(38) Haider, A.; Ijaz, M.; Imran, M.; Naz, M.; Majeed, H.; Khan, J. A.; Ali, M. M.; Ikram, M. Enhanced Bactericidal Action and Dye Degradation of Spicy Roots' Extract-Incorporated Fine-Tuned Metal Oxide Nanoparticles. *Appl. Nanosci.* **2020**, *10*, 1095−1104.
(39) Abagyan, R.; Totrov, M. Biased Probability Monte Carlo Conformational Searches and Electrostatic Calculations for Peptides and Proteins. *J. Mol. Biol.* **1994**, *235*, 983−1002.
(40) Lee, N. L. S.; Yuen, K. Y.; Kumana, C. R. β-Lactam Antibiotic and β-Lactamase Inhibitor Combinations. *JAMA* **2001**, *285*, 386−388.
(41) Drawz, S. M.; Bonomo, R. A. Three Decades of β-Lactamase Inhibitors. *Clinical Microbiology Reviews* **2010**, *23*, 160−201.
(42) Ushiyama, F.; Amada, H.; Takeuchi, T.; Tanaka-Yamamoto, N.; Kanazawa, H.; Nakano, K.; Mima, M.; Masuko, A.; Takata, I.; Hitaka, K.; Iwamoto, K.; Sugiyama, H.; Ohtake, N. Lead Identification of 8-(Methylamino)-2-Oxo-1,2-Dihydroquinoline Derivatives as DNA Gyrase Inhibitors: Hit-to-Lead Generation Involving Thermodynamic Evaluation. *ACS Omega* **2020**, *5*, 10145−10159.
(43) Barelier, S.; Eidam, O.; Fish, I.; Hollander, J.; Figaroa, F.; Nachane, R.; Irwin, J. J.; Shoichet, B. K.; Siegal, G. Increasing Chemical Space Coverage by Combining Empirical and Computational Fragment Screens. *ACS Chem. Biol.* **2014**, *9*, 1528−1535.
(44) Panchaud, P.; Bruyère, T.; Blumstein, A. C.; Bur, D.; Chambovey, A.; Ertel, E. A.; Gude, M.; Hubschwerlen, C.; Jacob, L.; Kimmerlin, T.; Pfeifer, T.; Prade, L.; Seiler, P.; Ritz, D.; Rueedi, G. Discovery and Optimization of Isoquinoline Ethyl Ureas as Antibacterial Agents. *J. Med. Chem.* **2017**, *60*, 3755−3775.
(45) Paramarta, V.; Taufik, A.; Munisa, L.; Saleh, R.Sono-and Photocatalytic Activities of SnO2 Nanoparticles for Degradation of Cationic and Anionic Dyes. *AIP Conference Proceedings*; American Institute of Physics Inc., 2017; Vol. *1788*.
(46) Kaizra, S.; Bellal, B.; Louafi, Y.; Trari, M. Improved Activity of SnO for the Photocatalytic Oxygen Evolution. *J. Saudi Chem. Soc.* **2018**, *22*, 76−83.
(47) Munawar, T.; Nadeem, M. S.; Mukhtar, F.; Rehman, M. N. U.; Riaz, M.; Batool, S.; Hasan, M.; Iqbal, F. Transition Metal-Doped SnO2 and Graphene Oxide (GO) Supported Nanocomposites as Efficient Photocatalysts and Antibacterial Agents. *Environ. Sci. Pollut. Res.* **2022**, *29*, 90995.
(48) Reddy Channu, V. S.; Ravichandran, D.; Rambabu, B.; Holze, R. Carbon and Functionalized Graphene Oxide Coated Vanadium Oxide Electrodes for Lithium Ion Batteries. *Appl. Surf. Sci.* **2014**, *305*, 596−602.
(49) Fu, C.; Zhao, G.; Zhang, H.; Li, S. Evaluation and Characterization of Reduced Graphene Oxide Nanosheets as Anode Materials for Lithium-Ion Batteries. *Int. J. Electrochem. Sci.* **2013**, *8*, 6269−6280.
(50) Zhan, S.; Li, D.; Liang, S.; Chen, X.; Li, X. A Novel Flexible Room Temperature Ethanol Gas Sensor Based on SnO2 Doped Poly-

https://doi.org/10.1021/acsomega.2c07460
ACS Omega 2023, 8, 5808−5819

Diallyldimethylammonium Chloride. *Sensors (Switzerland)* **2013**, *13*, 4378−4389.
(51) Rashad, M. M.; Ismail, A. A.; Osama, I.; Ibrahim, I. A.; Kandil, A. H. T. Photocatalytic Decomposition of Dyes Using ZnO Doped SnO2 Nanoparticles Prepared by Solvothermal Method. *Arab. J. Chem.* **2014**, *7*, 71−77.
(52) Adjimi, A.; Zeggar, M. L.; Attaf, N.; Aida, M. S. Fluorine-Doped Tin Oxide Thin Films Deposition by Sol-Gel Technique. *J. Cryst. Process Technol.* **2018**, *08*, 89−106.
(53) Wang, Q.; Zhang, J.; Wang, A. Preparation and Characterization of a Novel PH-Sensitive Chitosan-g-Poly (Acrylic Acid)/Attapulgite/Sodium Alginate Composite Hydrogel Bead for Controlled Release of Diclofenac Sodium. *Carbohydr. Polym.* **2009**, *78*, 731−737.
(54) Ikram, M.; Shahzadi, I.; Haider, A.; Hayat, S.; Haider, J.; Ul-Hamid, A.; Shahzadi, A.; Nabgan, W.; Dilpazir, S.; Ali, S. Improved Catalytic Activity and Bactericidal Behavior of Novel Chitosan/V2O5 Co-Doped in Tin-Oxide Quantum Dots. *RSC Adv.* **2022**, *12*, 23129−23142.
(55) Tran, V. H.; Ambade, R. B.; Ambade, S. B.; Lee, S. H.; Lee, I. H. Low-Temperature Solution-Processed SnO2 Nanoparticles as a Cathode Buffer Layer for Inverted Organic Solar Cells. *ACS Appl. Mater. Interfaces* **2017**, *9*, 1645−1653.
(56) Skrabania, K.; Miasnikova, A.; Bivigou-Koumba, A. M.; Zehm, D.; Laschewsky, A. Examining the UV-Vis Absorption of RAFT Chain Transfer Agents and Their Use for Polymer Analysis. *Polym. Chem.* **2011**, *2*, 2074−2083.
(57) Lozovskis, P.; Jankauskaitė, V.; Guobienė, A.; Kareivienė, V.; Vitkauskienė, A. Effect of Graphene Oxide and Silver Nanoparticles Hybrid Composite on p. Aeruginosa Strains with Acquired Resistance Genes. *Int. J. Nanomedicine* **2020**, *15*, 5147−5163.
(58) Madhu, G.; Biju, V. Effect of Ni2+ and O2- Vacancies on the Electrical and Optical Properties of Nanostructured Nickel Oxide Synthesized through a Facile Chemical Route. *Phys. E Low-dimens. Syst. Nanostruct.* **2014**, *60*, 200−205.
(59) Iqbal, S.; Javed, M.; Bahadur, A.; Qamar, M. A.; Ahmad, M.; Shoaib, M.; Raheel, M.; Ahmad, N.; Akbar, M. B.; Li, H. Controlled Synthesis of Ag-Doped CuO Nanoparticles as a Core with Poly(Acrylic Acid) Microgel Shell for Efficient Removal of Methylene Blue under Visible Light. *J. Mater. Sci. Mater. Electron.* **2020**, *31*, 8423−8435.
(60) Ahmed, A. S.; Shafeeq, M. M.; Singla, M. L.; Tabassum, S.; Naqvi, A. H.; Azam, A. Band gap narrowing and fluorescence properties of nickel doped SnO2 nanoparticles. *J. Lumin.* **2011**, *131*, 1−6.
(61) Jiang, Z. J.; Liu, C. Y.; Sun, L. W. Catalytic Properties of Silver Nanoparticles Supported on Silica Spheres. *J. Phys. Chem. B* **2005**, *109*, 1730−1735.
(62) Khan, M. M.; Lee, J.; Cho, M. H. Au@TiO2 Nanocomposites for the Catalytic Degradation of Methyl Orange and Methylene Blue: An Electron Relay Effect. *J. Ind. Eng. Chem.* **2014**, *20*, 1584−1590.
(63) Saha, J.; Begum, A.; Mukherjee, A.; Kumar, S. A Novel Green Synthesis of Silver Nanoparticles and Their Catalytic Action in Reduction of Methylene Blue Dye. *Sustain. Environ. Res.* **2017**, *27*, 245−250.
(64) Guan, Y.; Yu, H. Y.; Abdalkarim, S. Y. H.; Wang, C.; Tang, F.; Marek, J.; Chen, W. L.; Militky, J.; Yao, J. M. Green One-Step Synthesis of ZnO/Cellulose Nanocrystal Hybrids with Modulated Morphologies and Superfast Absorption of Cationic Dyes. *Int. J. Biol. Macromol.* **2019**, *132*, 51−62.
(65) Bari, A.; Ikram, M.; Haider, A.; Ul-Hamid, A.; Haider, J.; Shahzadi, I.; Nazir, G.; Shahzadi, A.; Imran, M.; Ghaffar, A. Evaluation of Bactericidal Potential and Catalytic Dye Degradation of Multiple Morphology Based Chitosan/Polyvinylpyrrolidone-Doped Bismuth Oxide Nanostructures. *Nanoscale Adv.* **2022**, *4*, 2713−2728.
(66) Li, X.; Feng, Y.; Li, H.; Zhang, Q. Effect of Anionic Groups on the Antibacterial Activity of Magnesium Oxide Nanoparticles. *Colloids Surfaces A Physicochem. Eng. Asp.* **2022**, *635*, 127978.
(67) Shahzadi, I.; Islam, M.; Saeed, H.; Haider, A.; Shahzadi, A.; Haider, J.; Ahmed, N.; Ul-Hamid, A.; Nabgan, W.; Ikram, M.; Rathore, H. A. Formation of Biocompatible MgO/Cellulose Grafted Hydrogel for Efficient Bactericidal and Controlled Release of Doxorubicin. *Int. J. Biol. Macromol.* **2022**, *220*, 1277−1286.
(68) Ikram, M.; Naeem, M.; Zahoor, M.; Hanafiah, M. M.; Oyekanmi, A. A.; Ullah, R.; Farraj, D. A. A.; Elshikh, M. S.; Zekker, I.; Gulfam, N. Biological Degradation of the Azo Dye Basic Orange 2 by Escherichia Coli: A Sustainable and Ecofriendly Approach for the Treatment of Textile Wastewater. *Water* **2022**, *14*, 2063.
(69) van der Zee, F. P.; Bouwman, R. H. M.; Strik, D. P. B. T. B.; Lettinga, G.; Field, J. A. Application of Redox Mediators to Accelerate the Transformation of Reactive Azo Dyes in Anaerobic Bioreactors. *Biotechnol. Bioeng.* **2001**, *75*, 691−701.
(70) Moir, D.; Masson, S.; Chu, I. Structure-Activity Relationship Study on the Bioreduction of Azo Dyes by Clostridium Paraputrificum. *Environ. Toxicol. Chem.* **2001**, *20*, 479−484.

Recommended by ACS

Modified Graphite Pencil Electrode Based on Graphene Oxide-Modified Fe_3O_4 for Ferrocene-Mediated Electrochemical Detection of Hemoglobin
Abdelaziz Elgamouz, Kamrul Hasan, *et al.*
MARCH 24, 2023
ACS OMEGA
READ

Biomass-Based Carbon Dots for Fe^{3+} and Adenosine Triphosphate Detection in Mitochondria
Samran Durrani, Fengming Lin, *et al.*
DECEMBER 20, 2022
ACS APPLIED NANO MATERIALS
READ

Bovine Serum Albumin-Coated Ceria Nanoparticles Activate the TGF-β Signaling Pathway for Periodontal Bone Regeneration
Xiang Meng, Lei Zhang, *et al.*
MARCH 21, 2023
ACS APPLIED NANO MATERIALS
READ

Proteomic Analysis of the Inflorescence Stem Mechanical Strength Difference in Herbaceous Peonies (*Paeonia lactiflora* Pall.)
Yan Sun, Chengzhong Li, *et al.*
SEPTEMBER 26, 2022
ACS OMEGA
READ

Get More Suggestions >

https://doi.org/10.1021/acsomega.2c07460
ACS Omega 2023, 8, 5808−5819